International Journal of Modelling and Simulation

www.tandfonline.com/journals/tjms20

(Editor-in-Chief: Professor Jie Shen - University of Michigan - Dearborn, USA)

Accepted July 14th 2023

Computation of micropolar nanofluid from a wedge with heterogeneous carbon/metallic nanoparticles, viscous dissipation and heat sink/source: Rheological nanocoating flow simulation

J. C. Umavathi[1*], Mahesh Ashok Kumar[1] and O. Anwar Bég[2]

[1]Department of Mathematics, Gulbarga University, Gulbarga-585 106, Karnataka, INDIA.
[2]Multi-Physical Engineering Sciences Group, Aeronautical/Mechanical Engineering, Salford University, School of Science, Engineering and Environment (SEE), Manchester, M54WT, UK.
**Corresponding author- email: drumavathi@rediffmail.com*

Abstract

Motivated by nanotechnological coating applications, a theoretical study is presented for the laminar, steady-state, incompressible nonlinear boundary layer flow of a non-Newtonian nanofluid external to a wedge-shaped configuration. The wedge surface is assumed to be isothermal. The Eringen micropolar model is deployed for rheological properties of the nanofluid. A Tiwari-Das nanoscale formulation is utilized in order to study specific nanoparticles and volume fraction effects. The dimensionless, transformed, coupled momentum, angular momentum (micro-rotation) and thermal perimeter layer equations are solved with the efficient MATLAB bvp4c numerical scheme. Validation with earlier studies is conducted. Aqueous-based nano-polymers are examined with either metallic/metallic oxide (copper, silver, titania) or carbon-based (diamond) nanoparticles. The influence of Hartree pressure gradient parameter (m), Eringen vortex viscosity (micropolar) parameter (K), nanoparticle volume fraction (ϕ), heat absorption (sink) parameter (Φ), Prandtl number (Pr) and nanoparticle type on velocity (F'), angular velocity (H), temperature (θ), skin friction function and Nusselt number function are visualized graphically and in tables. Temperature is strongly elevated with increasing micropolar parameter and nanoparticle volume fraction. Angular velocity (micro-rotation) is damped near the wedge surface with increment in volume fraction but further from the wall the reverse effect is observed. Velocity is boosted with increasing nanoparticle volume fraction. Temperatures are elevated with heat source (generation) but suppressed with heat sink

(absorption). Increasing Eckert number (dissipation) strongly enhances temperature and thermal boundary layer thickness. Temperatures are a maximum for silver and progressively lower for copper, diamond and with a minimum for titania. Skin friction is boosted with pressure gradient parameter whereas Nusselt number is depleted. Nusselt number is observed to be a maximum for diamond whereas it is a minimum for silver.

Keywords: *Nanofluids; Micropolar model; rheology; Tiwari-Das model; volume fraction; silver; copper; diamond; titania; viscous heating; heat source/sink; MATLAB bvp4c, Coating systems; Wedge.*

1. Introduction

Nanotechnology has revolutionized numerous applications in the 21st century. It has infiltrated into renewable energy systems (e. g. solar, geothermal), propulsion fuels, medicine, marine and manufacturing technology [1]. Numerous materials are being engineered at the nanoscale, in order to provide enhanced functionality, durability and ecologically- compatibility. Nanomaterials feature a diverse range of techniques for embedding nanoscale properties such as carbon nanotubes, graphene sheets, nano-shells, nanowires and nanoparticles. A subset of nanomaterials known as nanofluids [2] were introduced by doping conventional working fluids with metallic or carbon nanoparticles. These colloidal suspensions were demonstrated to enhance thermal conductivity and achieve superior thermal performance in a range of applications in automotive and industrial systems. Nanoparticles have more recently been implemented in designing more robust coatings for engineering components. Many different combinations have been studied including indium tin oxide nanoparticles with polymer base fluid [3] and TiO_2 nanoparticle layers [4], SnO_2: Sb (ATO) and In_2O_3: Sn (ITO) nanoparticles [5], clay and zinc oxide nanoparticles for plastic coatings [6] and polycaprolactone nanocomposites for thin film sheets [7]. These studies have shown that with judicious volume fraction selection, significant improvement in the stability and protective characteristics (e. g. anti-bacterial, anti-corrosion, abrasion resistance etc) can be achieved in nanofluid coatings. In conjunction with extensive laboratory-based studies, mathematical modelling of nanofluid coating flows has also stimulated much attention in recent years. Two popular approaches have been embraced in this

context. The first utilizes Buongiorno's model [8] which is a two-component nanoscale formulation and includes both heat and mass (nanoparticle) diffusion equations in addition to a momentum equation. However, while several important nanoscale mechanisms are included in this approach (e. g. Brownian dynamics and thermophoretic body force effects), it does not provide a framework for investigating specific nanoparticle materials and doping percentages. Tiwari and Das [9] introduced an alternative formulation based on Maxwell-Garnetts theory in which relationships were given for density, viscosity and thermal conductivity as functions of nanoparticle volume fraction. Although only momentum and heat transfer can be simulated with the Tiwari-Das model (since it neglects a nanoparticle species diffusion equation), nevertheless it provides a good framework for modelling the relative performance of different nanoparticle (and base fluids) in realistic flows. Both methodologies have been lucidly reviewed for many technological systems by Minkowycz et al. [10]. External coating flows frequently feature boundary layers which may be steady or unsteady, and many different types of systems arise such as stagnation flow deposition, stretching/contracting substrates, curved walls and wedges. In the context of nanofluid coating flows, Khaliq et al. [11] used the Tiwari-Das model to understand roll-coating of viscous nanofluid from a flat porous sheet. They showed that with increasing nanoparticle volume fraction, thermal characteristics and pressure gradient are enhanced. Ahmadian et al. [12] used the homotopy analysis method (HAM) to investigate the Ag-MgO hybrid nanoliquid coating flow on a wavy spinning disk, noting that the combination of hybrid nanoparticles (silver and magnesium-oxide) achieves a substantial improvement in thermal properties and heat transmission rate at the disk surface. Karim et al. [13] used COMSOL Multiphysics finite element software to simulate the heat transfer performance of graphite-dispersed Li_2CO_3-K_2CO_3 nanoparticles in saline base fluid for solar collector systems. They observed that a higher operating temperature is achieved compared to other working fluids.

The above studies considered nanofluids to be Newtonian in nature. However, many studies have identified that depending on the volume fraction of nanoparticles in base fluids, rheological characteristics may arise. Kim et al. [14] identified significant modifications in thermal and viscosity characteristics of nanofluids due to rheological properties including shear-thinning, viscoplasticity and volume fraction dependence. To accurately simulate the rheological behaviour of nanofluids, therefore, a non-Newtonian model is required. Many such models are

available. Rawat et al. [15] investigated the non-Fourier viscoelastic nanofluid convective reactive flow with the Oldroyd-B non-Newtonian model. Further studies include Umavathi and Bég [16] who applied the Stokes polar (couple stress) model for thermal stability in nanofluid-saturated porous media. With the exception of the couple stress model, the above non-Newtonian model are unable to represent the micro-structural characteristics of nanofluids, nano-polymers etc. The presence of suspended particles which can spin independently requires a more sophisticated rheological framework. A Special case of micromorphic fluid was developed by Eringen [17]. This model enables features microelements with a micro-rotation (gyration) vector which allows angular momentum to be simulated at the microscale. The micro-elements are small rigid cells which cannot deform but can spin and support surface and couple stresses. Micropolar theory has been deployed in an impressive range of applications since it robustly simulates actual behavior of complex liquids including lubricants, polymeric coatings, bacterial slime, blood, paints, liquid crystal suspensions, and also geomorphological fluids (muds, sediments). It is also ideal for boundary layer flows and produces a separate angular momentum (micro-rotation) boundary layer, distinct from the linear momentum boundary layer (velocity). Some recent applications of micropolar fluid mechanics include Ali et al. [18] (on bacterial gliding slime dynamics), Bég et al. [19] (on coating flows with magneto-micropolar functional materials), and Shamshuddin et al. [20] (on reactive periodic coating heat transfer). All these studies have utilized numerical methods such as spectral and finite element methods, MATLAB and finite difference techniques to accommodate the strong nonlinearity of micropolar boundary layer transport. They have also shown that the Newtonian classical case may be retrieved from the general micropolar model by neglecting vortex viscosity effects. Other studies have combined the micropolar model with various non-Newtonian formulations to expand the range of rheological behaviour which can be simulated in a single model. Micropolar convective heat transfer using Jeffery's through a cone was discussed by Madhavi et al. [21]. Abdul Gaffar et al. [22] developed Eyring-Powell model combining with Eringen micropolar to study coatings.

More recently engineers have combined micropolar and nanofluid models to provide a more comprehensive framework for simulating the rheological behaviour of nanofluids. The time-dependent bioconvection of micropolar nanofluid fluid was researched by Latiff et al. [22]. Higher volume fraction however boosts temperatures, micro-rotation and skin friction. Gumber

et al. [24] used $45^{th}/5^{th}$ order Runge-Kutta methods to compute the magneto-convective micropolar CuO-Ag/water hybrid nanofluid. They also studied the influence of different nanoparticle shape factors, wall suction/injection and micro-element wall concentration. Further studies include Das and Duari [25] who studied chemically reacting micropolar nanofluid transport with Buongiorno's model. Hussanan et al. [26] used the Tiwari-Das nanoscale model to derive Laplace transform solutions for boundary layer flow of micropolar nanofluids in order to study the performance of five oxide nanoparticles. The grapheme oxide micropolar nanofluid generated higher temperature when compared with other oxide nanopartilces.

Falkner and Skan [27] introduced for the first time a boundary layer framework for two-dimensional wedge flows. This type of flow also arises in chemical engineering processing and coating dynamics [28] and based on this formulation a number of special cases can be studied, namely, flat plate (Blasius) flow, rear stagnation point flow, forward stagnation point flow, etc. Many studies have therefore examined non-Newtonian wedge flows in order to simulate different industrial coating materials. Reddy et al. [29] deployed a tangent hyperbolic shear-thinning model and Keller's box method to analyse non-Newtonian mixed convective boundary layer flow from an isothermal wedge with entropy generation. Uddin et al. [30] and Bég et al. [31] investigated the micropolar convection flow external to a wedge. All these investigations elaborated in detail the influence of the Hartree pressure gradient parameter and other effects on skin friction and Nusselt number. More recently several works have addressed the nanofluid dynamics external to a wedge. These include Gaffar et al. [32] (who considered a non-isothermal wedge surface and used the Buongiorno model), Xu and Chen [33] (who included wall suction/injection effects), Uddin et al. [34] (who included electromagnetic induction and wall slip effects). Tulu et al. [35] implemented a spectral quasilinearization method (SQLM) and the Tiwari-Das model to study the unsteady two-dimensional reactive dissipative heat and mass transfer flow of nanofluid from a moving wedge. They showed that local Nusselt number is depleted with increment in nanoparticle volume fraction, Prandtl number and Eckert number whereas local Sherwood number is boosted with a rise in nanoparticle volume fraction, unsteadiness, pressure gradient and chemical reaction parameters. Further investigations of nanofluid boundary layer flows from a wedge with the Tiwari-Das model include Khan et al. [36] (for aluminum alloy nanoparticle-water nanofluids) and Ullah et al. [37] (for viscoplastic

nanofluid convection from a translating wedge). The steady-state, incompressible, laminar, and axi-symmetric flow of micropolar nanofluid flowing between two porous disks was analysed by Rauf et al. [38]. They observed that micropolar fluids were beneficial in the enhancement of couple stresses and in the reduction of shear stresses. They also showed that thermophoretic and Brownian motion parameters exhibit opposite effects on concentration profiles and that the concentration field is enhanced by the activation energy parameter. Numerical and correlation analysis for flow of micropolar fluid induced by two rotating disks was also studied by Rauf et al. [39]. They established that the micro-rotational profiles along the tangential direction are initially reduced in the left half plane and then enhanced in the right half plane of the central region with elevation in Eringen's vortex viscosity parameter. The magnitude of the couple stresses along radial and tangential directions were also shown to be modified at the surface of the upper and lower disk with increased values of the microinertia inertial density parameter, whereas these couple stresses were reduced with an increment in values of the spin gradient viscosity parameter. Rauf et al. [40] further considered the unsteady three-dimensional MHD flow of the micropolar fluid over an oscillatory disk with Cattaneo-Christov double diffusion. They noted that micro-rotational axial velocity increases when the magnetic parameter increases and when the swirl parameter increases, the radial velocity increases. The dynamics of micropolar nanofluid slip flow from a stretchable disk with Arrhenius activation energy was investigated by Nawaz et al. [41]. They identified that the temperature is augmented by increasing the thermophoresis and Brownian movement parameters while the heat transport rate is reduced with both these nanoscale parameters. Concentration field was also found to be reduced with larger Brownian movement parameter while it was enhanced with higher thermophoresis parameter.

"A scrutiny of the scientific literature has proved that the micropolar nanofluid convection from a wedge with the collective effects of viscous heating, multiple carbon/metallic nanoparticles and heat generation or absorption effects, has not been addressed. This problem is of direct relevance to rheological nano-polymer coating flows and the formulation presented significantly extends previous works with several novelties. In the present article therefore, motivated by providing a more generalized formulation for complex nano-coating external transport phenomena, a mathematical model is developed for the laminar, steady-state, incompressible nonlinear

convective boundary layer flow of a micropolar nanofluid external to an isothermal wedge configuration. Viscous dissipation [42] and heat generation/absorption effects are included which are known to be significant in actual nano-polymeric flow processing. The assessment of both carbon-based and metallic nanoparticles also furnishes deeper insight into their relative benefits for coating operations and tuning the properties of finished products for deployment in a range of industries including biomedical and aerospace." A Tiwari-Das nanoscale formulation is utilized in order to study specific nanoparticles and volume fraction effects. The Eringen micropolar theory is perfectly compatible with nanofluid dynamics. Microelements are at the micron scale and spin. However, the nanoparticles are at the nanoscale, a thousandth smaller than micro-elements. There is no interference between the nanoparticles and microelements. Micropolar fluid mechanics is therefore compatible with nanofluid dynamics. The dimensionless, transformed, coupled momentum, angular momentum and thermal boundary layer equations with associated wall and free stream conditions are solved with the efficient MATLAB bvp4c numerical scheme. Verification with prior studies is included. The focus is aqueous-based nano-polymers. Several metallic/metallic oxides (copper, silver, titania) or carbon-based (diamond) nanoparticles are considered [43, 44, 45] since these offer enhanced anti-bacterial benefits for modern coatings. The influence *of Hartree pressure gradient parameter (m), Eringen vortex viscosity (micropolar) parameter (K), nanoparticle volume fraction (ϕ), sink parameter (Φ), Prandtl number (Pr) and nanoparticle material type* on velocity, angular velocity, temperature, skin friction function and Nusselt number function are visualized graphically and in tables. The novelty of the present work is therefore the consideration of a range of different nanoparticles *(silver, diamond, copper and titania)* for micropolar nanofluids and the inclusion of simultaneous viscous heating and heat source/sink effects.

2. Mathematical formulation

2.1 Micropolar constitutive equations

The flow equations describing micropolar fluid (body couples and body forces are absent) which is incompressible, may be stated, following Eringen [17] as:

$$\nabla.\vec{V} \tag{1}$$

$$\rho\left(\vec{V}.\nabla\vec{V}\right) = \left(\mu + \kappa\right)\nabla^2\vec{V} - \nabla p + \kappa\left(\nabla\times\vec{W}\right) \tag{2}$$

$$\rho\, j\left(\vec{V}.\nabla\vec{W}\right) = \kappa\left(\nabla\times\vec{W}\right) - 2\kappa\,\vec{W} + \left(\alpha' + \beta' + \gamma\right)\nabla\left(\nabla.\vec{W}\right) - \gamma\left(\nabla\times\nabla\times\vec{W}\right) \tag{3}$$

Here ρ is the micropolar fluid density, p is the fluid pressure, j is the micro-gyration and other parameters are same as in Uddin et al. [30].

2.2 Tiwari-Das nanoscale model

The Tiwari-Das nanofluid model [9] defines the modified dynamic viscosity, specific heat capacity and thermal conductivity using the following relations where $\left(\ \right)_f$ represents the base fluid, $\left(\ \right)_{nf}$ denotes the nanofluid and $\left(\ \right)_s$ corresponds to the solid nanoparticles e.g. diamond, copper, titania and silver:

$$\mu_{nf} = \mu_f\left(\left(1-\phi\right)^{2.5}\right)^{-1} \tag{4}$$

$$\left(\rho C_p\right)_{nf} = \phi\left(\rho C_p\right)_s + \left(1-\phi\right)\left(\rho C_p\right)_f \tag{5}$$

$$K_{nf} = K_f\left(\frac{2K_f + K_s - 2\phi\left(K_f - K_s\right)}{2K_f + K_s + \phi\left(K_f - K_s\right)}\right) \tag{6}$$

Here ρ denotes density and ϕ represents the volume fraction of nanoparticles. The modified properties appear in the model developed in the next section.

2.3 Governing equations for micropolar nanofluid convection from a wedge

The regime under study is displayed in Fig. 1. Steady, two-dimensional, viscous, incompressible, forced convective boundary layer flow of a micropolar nanofluid external to a two-dimensional wedge is studied. An $\left(x,\ y\right)$ coordinate system is adopted where the $x-$coordinate is along the wedge face and the y-coordinate is perpendicular to it. The nanofluid is assumed dilute and the nanoparticles and microelements do not interact. Local thermal equilibrium is assumed between the nanoparticles and the base fluid (micropolar liquid). Viscous heating and heat generation or absorption are included. The external velocity is defined as $U = c\,x^m$, where $c > 0$,

$m = \dfrac{\beta^*}{\left(2-\beta^*\right)}$ is the Hartree pressure gradient parameter which corresponds to $\beta^* = \dfrac{\Omega}{\pi}$ for a vertex angle Ω of the wedge.

Under the above approximations, the boundary layer equations for the coating flow are [31, 42]

Continuity

$$\frac{\partial u}{\partial x}+\frac{\partial v}{\partial y}=0 \tag{7}$$

$x-$ directional linear momentum equation (primary):

$$u\frac{\partial u}{\partial x}+v\frac{\partial v}{\partial y}=\left(\frac{\mu_{nf}+\kappa}{\rho_{nf}}\right)\left(\frac{\partial^2 u}{\partial y^2}\right)+\frac{\kappa}{\rho_{nf}}\frac{\partial N}{\partial y}+U\frac{dU}{dx} \tag{8}$$

$z-$ directional linear momentum equation (secondary):

$$u\frac{\partial w}{\partial x}+v\frac{\partial w}{\partial y}=\left(\frac{\mu_{nf}+\kappa}{\rho_{nf}}\right)\left(\frac{\partial^2 w}{\partial y^2}\right) \tag{9}$$

Angular momentum conservation equation (micro-rotation):

$$\rho_{nf}\ j\left(u\frac{\partial N}{\partial x}+v\frac{\partial N}{\partial y}\right)=\frac{\partial}{\partial y}\left(\gamma_{nf}\frac{\partial N}{\partial y}\right)-\kappa\left(\frac{\partial u}{\partial y}+2N\right) \tag{10}$$

Energy (heat) conservation:

$$\left(\rho c_p\right)_{nf}\left(u\frac{\partial T}{\partial x}+v\frac{\partial T}{\partial y}\right)=K_{nf}\left(\frac{\partial^2 T}{\partial y^2}\right)+\left(\mu_{nf}+\kappa\right)\left(\left(\frac{\partial u}{\partial y}\right)^2+\left(\frac{\partial w}{\partial y}\right)^2\right)+Q\left(T-T_\infty\right) \tag{11}$$

The wall and free stream boundary conditions are:

$$u=v=w=0,\quad N=-n\frac{\partial u}{\partial y},\quad q_w=-K_{nf}\frac{\partial T}{\partial y}\ \text{ at }\ y=0 \tag{12}$$

$$u\to U,\ w\to 0,\ N\to 0,\qquad T\to T_\infty\qquad \text{as}\ \ y\to\infty \tag{13}$$

Here: K_{nf} is the nanofluid thermal conductivity, $\left(\rho C_p\right)_{nf}$ is the specific heat capacity of the micropolar nanofluid, ρ_{nf} is density, T is temperature, Q heat generation/absorption parameter, T_∞ is free stream temperature, q_w is wall heat flux, $\gamma_{nf} = \left(\mu_{nf} + \frac{\kappa}{2}\right) j = \mu_{nf}\left(1+\frac{K}{2}\right) j$ where $K = \frac{\mu_f}{\kappa}$ is the Eringen micropolar material parameter and the other parameters are same as in Uddin et al. [30].

The primitive Eqns. (7)-(11) with associated boundary conditions (12) and (13) are strongly nonlinear. Their numerical solutions can be found by using the similarity variables

$$\eta = \sqrt{\frac{U\left(m+1\right)}{2\nu_{nf} x}}\ y\ ;\ \psi = \sqrt{\frac{2xU\nu_{nf}}{\left(m+1\right)}}\ F(\eta),\ \ w = U\ G(\eta),\ \ N = U\sqrt{\frac{(m+1)U}{2\nu_{nf} x}}\ H(\eta)$$

$$\theta(\eta) = \frac{K_{nf}\ (T-T_\infty)}{q_w}\sqrt{\frac{(m+1)U}{2\nu_{nf} x}},\ \ \Phi = \frac{2\,x\,Q(x)}{\left(\rho c_p\right)_{nf} U} \tag{14}$$

Here η (transverse coordinate), ψ (stream function), $H\left(\eta\right)$ (micro-rotation velocity), $F\left(\eta\right)$ (stream function), $G\left(\eta\right)$ (secondary velocity), $\theta(\eta)$ (temperature) and Φ (heat source/sink). Implementing the transformations (14) in Eqns. (7)-(11), the following self-similar coupled boundary layer equations emerge:

$$\left(1+K\left(1-\phi\right)^{2.5}\right)F''' + F\ F'' + K\ \left(1-\phi\right)^{2.5}\ H' - \frac{2m}{m+1}\left(1-\left(F'\right)^2\right) = 0 \tag{15}$$

$$\left(1+K\left(1-\phi\right)^{2.5}\right)G'' + F\,G' - \frac{2m}{m+1}G\ F' = 0 \tag{16}$$

$$\left(1+\frac{K}{2}\left(1-\phi\right)^{2.5}\right)H''\ -\ \frac{2KI\,C_5}{\left(m+1\right)}\left(2H+F''\right) - \left(\frac{3m-1}{m+1}\right)H\,F' - F\,H' = 0 \tag{17}$$

$$\frac{C_1\ C_2\ C_3}{\mathrm{Pr}}\ \theta'' + \left[Ec\ \left(1+K\,C_1\right)\ C_2\ \left(\left(F''\right)^2 + \left(G'\right)^2\right) + \frac{C_3\,\Phi}{m+1}\right]\ \theta\ + \left(\frac{m-1}{m+1}\right)F'\theta + F\,\theta' = 0 \tag{18}$$

The resulting boundary conditions (12, 13) in *dimensionless* form are:

$$F(0) = 0\ ;\ F'(0) = 0\ ;\ G(0) = 0\ ;\ H(0) = -0.5\ F''(0)\ ;\ \theta' = -1 \tag{19}$$

$$F'(\infty) \to 1\ ;\ G(\infty) = H(\infty) = \theta(\infty) \to 0 \tag{20}$$

Here (') represents the derivative with respect to η, $u = \frac{\partial \psi}{\partial y}$ and $v = -\frac{\partial \psi}{\partial x}$, (which automatically satisfies the mass conservation Eqn. (7)) $I = \frac{\nu_f{}^2 \,\mathrm{Re}}{j\, U^2}$ (inertial parameter), $\mathrm{Re} = \frac{U\, x\, \rho_f}{\mu_f}$ (Reynolds number) and $Ec = \frac{U^2}{\left(C_p\right)_f \left(T - T_\infty\right)}$ (Eckert number). Furthermore, the nanofluid property constants are defined as:

$$C_1 = \left(1-\phi\right)^{2.5},\quad C_2 = \frac{\left(C_p\right)_f}{\left(C_p\right)_{nf}},\quad C_3 = \frac{\left(\rho C_p\right)_{nf}}{\left(\rho C_p\right)_f},\ C_4 = \frac{K_{nf}}{K_f},\ C_5 = \frac{\rho_f}{\rho_{nf}}. \tag{21}$$

In Eqn. (19), the micro-rotation boundary condition, $H\left(0\right) = -\,0.5\, F''\left(0\right)$ corresponds to the scenario of weak concentration of micro-elements at the wall (Eringen, [17]; Bég et al. [19]). Although other surface conditions are possible e. g. n = 0 and n = 1 which imply strong near-wall micro-element concentrations and turbulent flows, respectively, they are not considered in this study. The angular velocity boundary condition deployed is most suitable for laminar coating boundary layer flows. Characteristics at the wedge surface are critical in coating flow operations. Specifically, the gradients of primary and secondary velocity and temperature provide a good insight into momentum and heat transfer characteristics. The local skin friction coefficients and local Nusselt number are:

$$C_{fx} = \frac{\tau_w}{\frac{1}{2}\rho_{nf}U^2},\ C_{fz} = \frac{\tau_z}{\frac{1}{2}\rho_{nf}U^2} \text{ and } Nu = \frac{xq_w}{K_{nf}(T-T_\infty)} \tag{22}$$

Here:

$$\tau_w = \left[(\mu_{nf}+\kappa)\frac{\partial u}{\partial y} + \kappa N\right]_{y=0},\quad \tau_z = \left[(\mu_{nf}+\kappa)\frac{\partial w}{\partial y}\right]_{y=0} \text{ and } \quad q_w = -K_{nf}\frac{\partial T}{\partial y} \tag{23}$$

Therefore, the desired dimensionless primary, secondary skin frictions, and Nusselt number expressions emerge as:

$$c_{fx} = \sqrt{\frac{2(m+1)\ C_5}{\mathrm{Re}\, C_1}} \left(1+\frac{K}{2}\right) F''(0) \tag{24}$$

$$c_{fz} = \sqrt{\frac{2(m+1) C_5}{\mathrm{Re}\ C_1}} \left(1+K\, C_1\right) G'(0) \tag{25}$$

$$NU = \sqrt{\frac{(m+1) C_1 \mathrm{Re}}{2\ C_5}}\ \frac{1}{\theta(0)} \tag{26}$$

3. Numerical MATLAB solutions and validation

The nonlinear ordinary differential boundary value problem defined by Eqns. (15)-(20) can be solved by using various numerical methods including finite elements, finite difference, homotopy analysis, Adomian decomposition etc. Here we elect the MATLAB BVP4C (boundary value problems)) routine which uses the exceptionally accurate and stable Runge–Kutta–Merson numerical quadrature ("RK45 algorithm"). This technique has been applied to many multi-physical fluid dynamics problems e. g. triple diffusive convection [46] and magnetic squeeze films [47] in recent years and can accommodate any order of derivative. In MATLAB this quadrature is used to obtain solutions for stream function, secondary velocity, micro-rotation and temperature. BVP4C uses stepping formulae which are summarized in Umavathi et al. [47]. Further details are given in Kattan [48].

The algorithm relies on an iteration structure. BVP4C is a numerical platform that implements the Lobatto IIIa three-stage formula. This is a collocation formula which is formed by a polynomial collocation. It provides a C1-continuous solution that is fourth-order accurate uniformly in $x \in [a, b]$. The fourth-order formulae are given below:

$$k_1 = L\ \ f\left(x_n, y_n\right)$$

$$k_2 = L\ f\left(x_n+\frac{L}{2}, y_n + \frac{k_1}{2}\right)$$

$$k_3 = L\ f\left(x_n+\frac{L}{2}, y_n + \frac{k_2}{2}\right)$$

$$k_4 = L\, f\left(x_n+L, y_n + k_3\right)$$

$$y_{n+1} = y_n + \frac{k_1}{6} + \frac{k_2}{3} + \frac{k_3}{3} + \frac{k_4}{6} + O\left(L^5\right) \tag{27}$$

where $L = \left(x_{i+1} - x_i\right)$ represents the size of each subinterval.

The crucial part in solving the bvp4c is the variation step and early guessing of the mesh point. Besides, the efficiency will eventually depend on the programmer ability in providing the algorithm with an initial guess for the solution. We created two folders, namely, "code a" and "code b", for the trial-and-error initial guess and continuous iterations that approximate closely to the initial guess, respectively. The above-described computing approach cannot be used without transforming the higher-order differential equations to differential equations of order one. The mathematical process is described as follows:

$$\left.\begin{array}{l} F = y_1, \quad F' = y_2, \quad F'' = y_3 \\ G = y_4, \quad G' = y_5 \\ H = y_6, \quad H' = y_7 \\ \theta = y_8, \quad \theta' = y_9 \end{array}\right\} \tag{28}$$

$$F'' = -\frac{1}{(1+K\,C_1)}\left[K\,C_1\,y_7 - \frac{2\,m}{(m+1)}\left(y_2{}^2 - 1\right) + y_1\,y_3\right] \tag{29}$$

$$G'' = -\frac{1}{(1+K\,C_1)}\left[-\frac{2\,m}{(m+1)}\,y_4\,y_2 + y_1\,y_5\right] \tag{30}$$

$$H'' = -\frac{1}{(1+0.5\,K\,C_1)}\left[-\frac{2\,K\,I}{(m+1)}C_5\left(2\,y_6 + y_3\right) - \frac{(3m-1)}{(m+1)}\,y_2\,y_6 + y_1\,y_7\right] \tag{31}$$

$$\theta'' = -\frac{\Pr}{C_4\,C_2\,C_1}\left[y_1\,y_9\left\{\frac{m-1}{m+1}y_2 + (1+K\,C_1)C_2\,Ec\left(y_3{}^2 + y_5{}^2\right) + \frac{C_2\,C_5}{m+1}\,\Phi\right\}\,y_8\right] \tag{32}$$

The corresponding boundary conditions become

$$\left.\begin{array}{l} y_1(0) = 0; \quad y_2(0) = 0; \quad y_4(0) = 0\,; \quad y_6(0) = -\dfrac{y_3(0)}{2}; \quad y_9(0) = -1 \end{array}\right\} \quad at\ \eta = 0 \tag{33}$$

$$\left.\begin{array}{l} y_2(\infty) \to 1;\ y_4(\infty) \to 0;\ y_6(\infty) \to 0;\ y_8(\infty) \to 0 \end{array}\right\} \quad as\ \eta \to \infty \tag{34}$$

Some commands in handling the function such as "@odeBVP" and "@odeBC" are from the syntax of the solver "sol = bvp4c" (@OdeBVP, @OdeBC, solinit, options). The iterative process is carried out until an accuracy of 10^{-6} is achieved which is obtained for the values of $\eta_\infty = 5$

(infinity boundary condition) and $\Delta\eta = 0.001$ (step size). The numerical results obtained from the solver are then plotted as graphs.

To validate the MATLAB bvp4c solutions, a comparison has been made with several previous studies from the literature [30, 50, 51, 52]. In these benchmark studies viscous heating, nanofluid and heat source/sink effects were neglected. The comparisons are shown in Tables 1 and 2 for primary skin friction $\left(\frac{C_{fx}\sqrt{\mathrm{Re}}}{2}\right)$ and reduced Nusselt number $\left(\frac{Nu}{\sqrt{\mathrm{Re}}}\right)$ respectively. A very wide range of Prandtl numbers is included in Table 2. In both Tables, the case $m=0$ is examined (Blasius flow). Excellent agreement is captured and confidence in the MATLAB bvp4c is highly justifiably. In Tables 1 and 2 the values chosen are $I = 0.5,\ \phi = 0,\ K = 0,\ m = 0,\ C_1 = C_2 = C_3 = C_4 = C_5 = 1.0,\ \Phi = 0.0,\ Ec = 0.0,\ \mathrm{Pr} = 6.0$

4. Results and discussion

Extensive visualization of MATLAB solutions is given in Figs. 2-7. Table 3 also documents the values of $\left(\frac{C_{fx}\sqrt{\mathrm{Re}}}{2}\right)$ and $\left(\frac{Nu}{\sqrt{\mathrm{Re}}}\right)$ for all key parameters. In all the plots, the following data is prescribed (unless otherwise indicated): $I = 0.5,\ \phi = 0.01,\ K = 0.5,\ m = 0.3333,\ \Phi = -0.5,\ Ec = 0.5,\ \mathrm{Pr} = 6.0$. This corresponds to water as base fluid and copper nanoparticles (Hussain [1]). Generalized wedge flow is considered $(m = 0.3333)$ and heat sink $(\Phi = -0.5)$ strong dissipation $(Ec = 0.5)$ and these correspond closely to actual nano-polymer flow coating data (Hussain and Thomas [65]).

Figures 2a-c exhibit (a) primary velocity (F') (b) angular velocity (H) and (c) temperature (θ) for various pressure gradient parameter values (m). The case $m = 0$ implies Blasius flow past a flat horizontal surface (for which $U = c\,x^m \rightarrow U = c$) and $m = 1$ corresponds to forward stagnation point flow adjacent to a vertical surface (i. e. linear free stream velocity variation with

axial distance (for which $U = c\,x^m \rightarrow U = c\,x$). Figure 2a shows that former $(m = 0)$ linear primary velocity is a minimum whereas for the latter $(m = 1)$ it is a maximum.

Velocity is generally elevated with increase in pressure gradient parameter since pressure gradient assists the momentum development on the wall and encourages boundary layer growth. Wedge flow $(m > 0)$ therefore produces strong flow acceleration relative to flat plate flow whereas maximum flow acceleration is only achieved with $m = 1$. The trend in profiles is sustained at all values of η. There is no cross-over of profiles anywhere in the boundary layer. The parameter m features in the modified shear terms in the primary momentum Eqn. (15), $\left(1 + K\left(1-\phi\right)^{2.5}\right) F''$ and $-\frac{2m}{m+1}\left(1-\left(F'\right)^2\right)$, and will evidently modify shear characteristics considerably. Momentum boundary layer thickness is generally reduced with increasing pressure gradient parameter values (m). It is also delightful to figure that as the value of m is increased the profiles evolve from a linear growth to increasingly parabolic i. e. nonlinear topologies. This has also been observed in other wedge flow boundary layer nanofluid studies e.g. [36, 37]. In all cases the magnitudes of primary velocity are positive indicating that flow reversal never occurs in the boundary layer. Figure 2b shows that angular velocity is also strongly influenced by pressure gradient parameter values (m). Initially near the wall (wedge surface) there is a very strong decrement in micro-rotation (H) indicating that micro-elements rotate increasingly in the reverse direction. The implication is that for flat plate scenario $(m = 0)$ and also wedge geometries $(0 < m < 1)$ and the forward stagnation flow case $(m = 1)$, close to the wall there is increasing reverse spin and angular deceleration. However, with further distance from the wall, angular acceleration is achieved and sustained into the free stream. The pressure gradient parameter (m) arises in the terms, $\left(-\frac{2K\,I\,C_5}{(m+1)}\right) - \frac{2K\,I\,C_5}{(m+1)}\left(2\,H + F''\right) - \left(\frac{3m-1}{(m+1)}\right) H\,F'$ in the angular momentum boundary layer Eqn. (17). These terms are also strongly coupled with the primary momentum Eqn. (15). Micro-rotation therefore exhibits considerable sensitivity to the pressure gradient parameter. Maximum angular velocity corresponds to the flat plate case nearer the wall and to the forward stagnation flow case further from the wall. The wedge cases

$(0 < m < 1)$ fall in between these two extremities. Figure 2c depicts the distribution of temperature with various m values. There are several terms in the energy Eqn. (18) which also feature this parameter. Increment in m is observed to markedly boost the temperature magnitudes at all locations from the wall to the free stream. Profiles become increasingly parabolic in nature with higher m. For vanishing pressure gradient (flat plate case, $m = 0$) temperature is minimized. However, it is maximized for the $m = 1$ for which pressure gradient is strongest. The wedge case $(0 < m < 1)$ are intercalated between these other two cases. Thermal boundary layer thickness is therefore a maximum for the forward stagnation flow case and a minimum for the flat plate (Blasius) case.

Figure 3 illustrates the effect of K on (a) F' (b) H and (c) θ with transverse coordinate, η. Figure 3a reflect the decrease in F' with increment in K values. The Newtonian case i. e. $K = 0$ achieves maximum acceleration. With greater values of K there is stronger micropolarity of the nanofluid i. e. vortex viscosity is enhanced. This contributes to a reduction in momentum diffusion in F' which decelerates the flow. Therefore, the inclusion of micropolar effects produces more accurate predictions for the primary velocity; the Newtonian model over-predicts the velocity and under-predicts the momentum boundary layer thickness. The drag-reducing properties of micropolar nanofluids are therefore confirmed and these have been identified also in Eringen [17] and many other studies [24]. Figure 3b, depicts a strong enhancement in H, H is induced near the wedge surface i.e. wall with a rise in Eringen micropolar material parameter values (K). Profiles also grow linearly with transverse coordinate. However further from the wedge face, the pattern is opposite and there is a strong deceleration induced in angular velocity with increasing K values and profiles assume a parabolic form. The micropolar vortex viscosity effect is therefore dependent on the location in the boundary layer. Closer to the wedge surface the boost in micropolar material parameter encourages spin of the micro-elements, whereas further away the rotary motions are damped. Figure 3c shows that a strong boost in temperatures accompanies an increment in K. The Newtonian case $(K = 0)$ produces the minimal temperature i. e. a cooling effect relative to micropolar nanofluids. Increasing micropolar vortex viscosity strongly heats the regime, implying a hike in thermal diffusion and an associated elevation in thermal boundary layer

thickness. This will simultaneously produce a decrease in heat transfer rate to the wall with increasing micropolarity. Therefore, wall cooling of the coating flow will be achieved with micropolar nanofluids (this is desirable in polymer processing coatings as noted in Hussain and Thomas [52]) whereas Newtonian nanofluids will induce undesirable heating at the wall.

Figure 4 visualize the profiles for (a) primary velocity (F') (b) angular velocity (H) and (c) temperature (θ) for various nanoparticle volume fractions (ϕ) (copper nanoparticles in water). A distinct enhancement in primary velocity (Fig. 4a) is computed with increasing volume fraction at some distance from the wedge surface i. e., with increment in percentage doping of nanoparticles in the nano-polymer, there is clear acceleration in primary flow and associated reduction in momentum boundary layer thickness. The increasing presence of nanoparticles therefore assists momentum diffusion in the regime. The modification in nanofluid viscosity is therefore beneficial for coating flow dynamics. The case where nanoparticles are absent $(\phi = 0)$ produces the lowest magnitude of velocity and the maximum boundary layer thickness. A steady growth in primary velocity is computed from the wall to the free stream and backflow (negative velocity) is never witnessed. Near the wedge face, Fig. 4b reveals that increment in nanoparticle volume fraction produces a weak deceleration in micro-rotation i. e. angular velocities becoming increasingly negative and micro-elements spin faster in the reverse direction. Further into the boundary layer regime, transverse to the wedge surface, there is however a switchover in behavior. Beyond the critical point at $\eta \approx 1.1$, the angular velocity is accentuated with increasing volume fraction. The greater space available for gyratory motions enables a boost in angular velocity beyond the critical location with higher values of nanoparticle volume fraction. All angular velocity profiles tend smoothly to the free stream (maximum) value confirming excellent convergence in the MATLAB bvp4c computations. A significant elevation in temperature is observed with greater nanoparticle volume fractions (ϕ) in Fig. 4c. The thermal conductivity is significantly increased with nanoparticles. Thermal diffusion is assisted, and thermal boundary layer thickness is strongly increased. The nanoparticles therefore achieve the fundamental objective of thermal enhancement in the regime, as confirmed in numerous studies [1, 36, 37]. At higher volume fractions there is also a more parabolic nature to the temperature

distribution; at lower values it is generally a linear decay from the wall (wedge face) to the free stream.

Figure 5 displays the influence of heat source/sink parameter (Φ) on temperature (θ). This parameter arises in the term, $\left(\frac{C_3\ \Phi}{(m+1)}\right)\theta$ in the energy boundary layer Eqn. (18). This is an important effect in nanomaterials processing wherein a hot spot or cooling spot are present on the substrate being coated to enable manipulation of thermal energy. With increment in positive values of (Φ), heat generation effect is amplified so that the term, $\left(\frac{C_3\ \Phi}{(m+1)}\right)\theta$ makes a more prominent contribution to thermal diffusion. This significantly enhances temperatures throughout the regime. The converse effect is induced with elevation in negative values of (Φ), the heat sink (absorption) effect is amplified. The case of $\Phi \to 0$ implies an absence of either heat source or sink. This profiles naturally falls in between the heat source and heat sink cases. There is overall a marked enhancement in thermal boundary layer thickness with heat generation $(\Phi > 0)$ i. e. heating effect in the micropolar nanofluid coating and a decrement in thermal boundary layer thickness $(\Phi < 0)$ i. e. cooling effect. It is also noteworthy that sharper gradients in temperature are observed at higher values of positive or negative Φ although again all profiles converge smoothly in the free stream at maximum value of the transverse coordinate.

Figure 6 illustrates the evolution in temperature in the regime with increment in *Ec.* This parameter signifies the relative contribution of kinetic energy dissipated via internal friction in the micropolar nanofluid. It features in the term, $\left[Ec\,(1+K\,C_1)\,C_2\,(F'')^2+(G')^2\right]\theta$ in the heat Eqn. (18). Elevation in Ec amplifies this term and leads to a strong increment in temperatures throughout the boundary layer. Thermal boundary layer thickness is therefore substantially enhanced also with greater Eckert number. In the absence of viscous heating $Ec = 0$ and minimum temperatures are computed. The neglection of viscous dissipation therefore strongly underestimates actual temperatures arising in micropolar nanofluid coating flows. Viscous heating is known to be significant in polymer processing (Hussain and Thomas [52]) and the inclusion of this effect is therefore justified for more accurate simulations.

Figure 7 depicts the distribution in temperature for various nanoparticle types (silver, copper, diamond and titania). Maximum temperatures are observed for silver and are sustained at all values of transverse coordinate, although the greatest enhancement is at the wedge face. As nanoparticles are changed to copper, diamond and titania there is a progressive decrease in temperature and also thermal boundary layer thickness. Copper achieves the second highest temperatures. Diamond nanoparticles produce a weakly greater temperature than titania (titanium oxide metallic) nanoparticles. The latter are associated with the minimal temperatures. Overall thermal enhancement in the boundary layer coating regime is best with silver nanoparticles although copper is also quite effective, and these trends are attributable to the impressive thermal conductivities of these nanoparticles relative to diamond and titania.

Table 3 shows that with an increase in pressure gradient parameter (m), primary skin friction i. e. $\frac{C_{fx}\sqrt{\mathrm{Re}}}{2}$ is strongly enhanced whereas Nusselt number $\frac{Nu}{\sqrt{\mathrm{Re}}}$ is strongly suppressed. Highest heat transfer rate to the wall is therefore computed for $m = 0$ whereas the minimum heat transfer rate to the wall is produced for $m = 1$. The wedge case lies between these two extremities. An increase in micropolar material parameter, K induces a strong increase in primary skin friction $\frac{C_{fx}\sqrt{\mathrm{Re}}}{2}$ whereas it depletes the Nusselt number $\frac{Nu}{\sqrt{\mathrm{Re}}}$ magnitudes for the wedge case ($m = 0.3333$ with 1% nanoparticle doping). Strongly micropolar nanofluids therefore shear faster along the wedge face whereas they produce a decrement in heat transfer to the wall (cooling effect). Both primary skin friction and Nusselt number are depleted with increment in ϕ. Stronger doping of nanoparticles therefore decelerates the flow along the wedge wall and also suppresses the rate of heat transferred to the wall i. e. cooling is produced (since temperatures within the boundary layer are increased). Maximum primary skin friction is computed for diamond, followed by titania, then copper and a minimum for silver. A similar trend is computed for the Nusselt number i. e. the highest magnitude is for diamond, followed by titania, then copper and again the lowest magnitude is observed for silver.

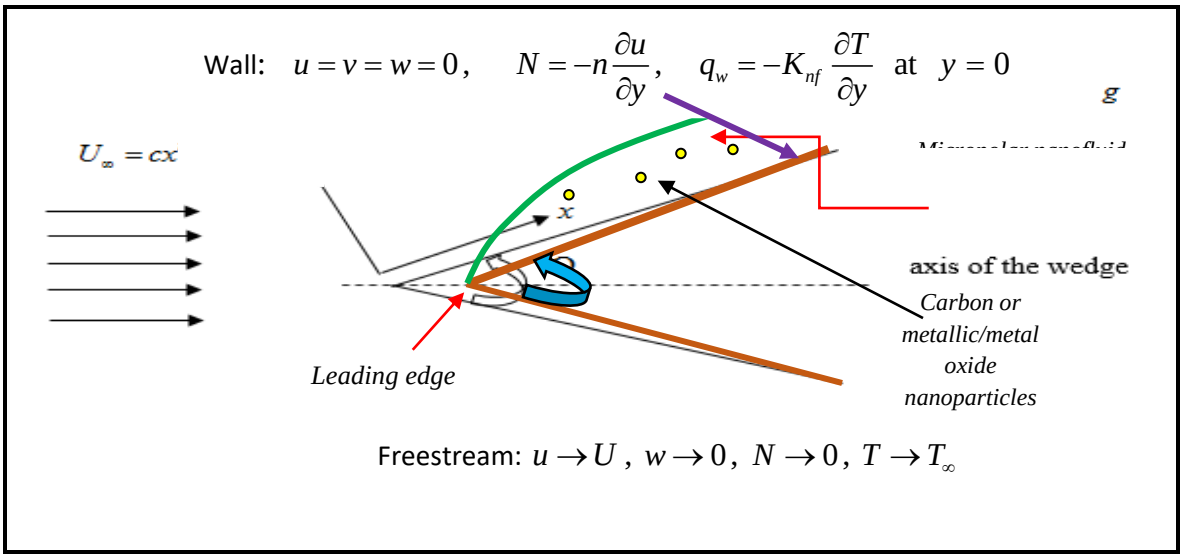

Figure 1. Schematic diagram for micropolar nanofluid flow external to a wedge

(a)

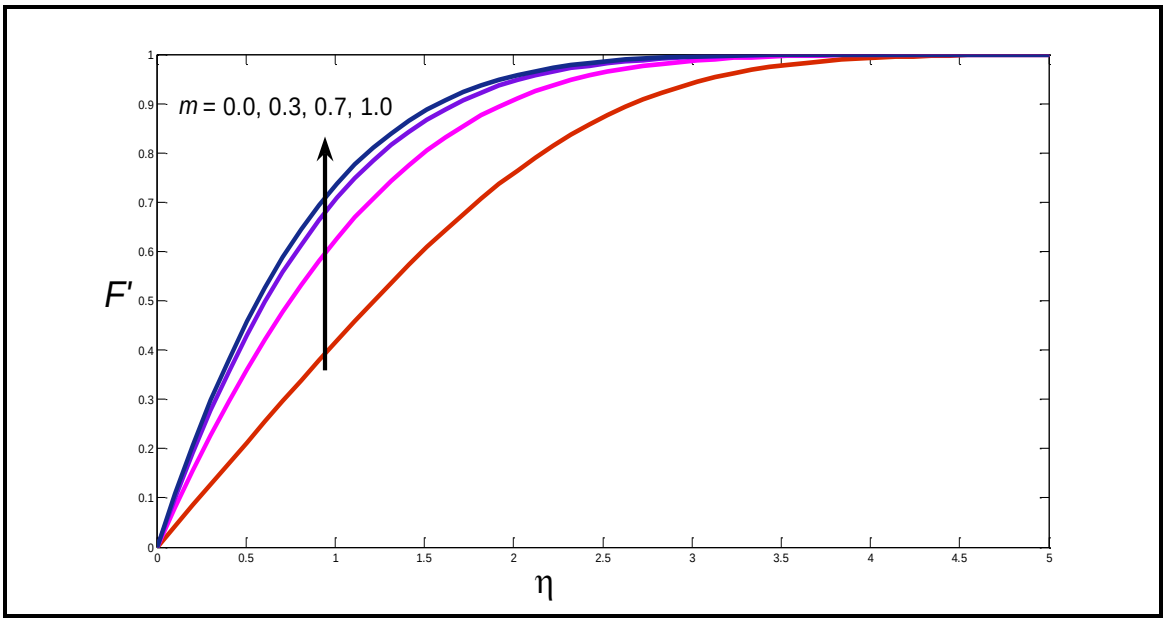

(b)

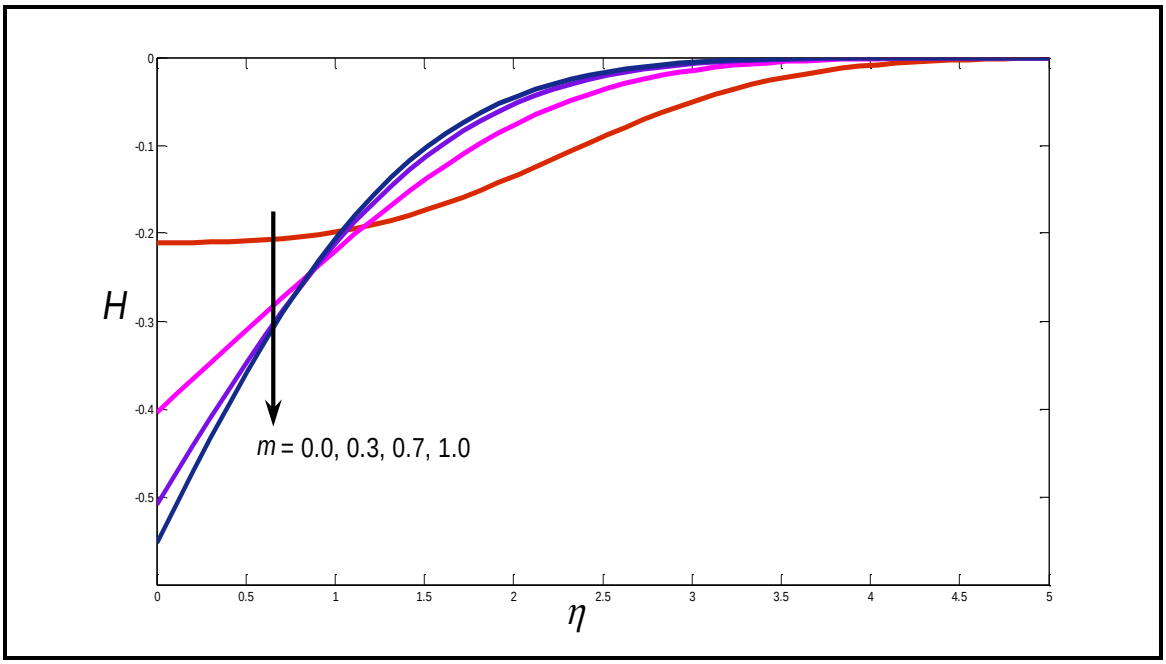

(c)

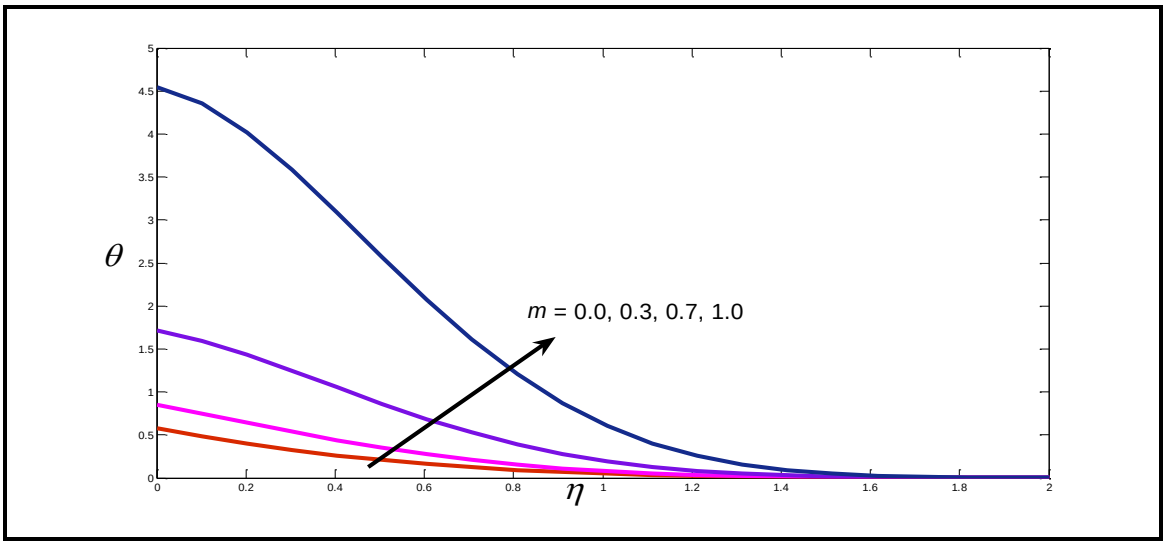

Figure 2. Profiles for (a) primary velocity (F') (b) angular velocity (H) and (c) temperature (θ) for various pressure gradient parameter values (m)

(a)

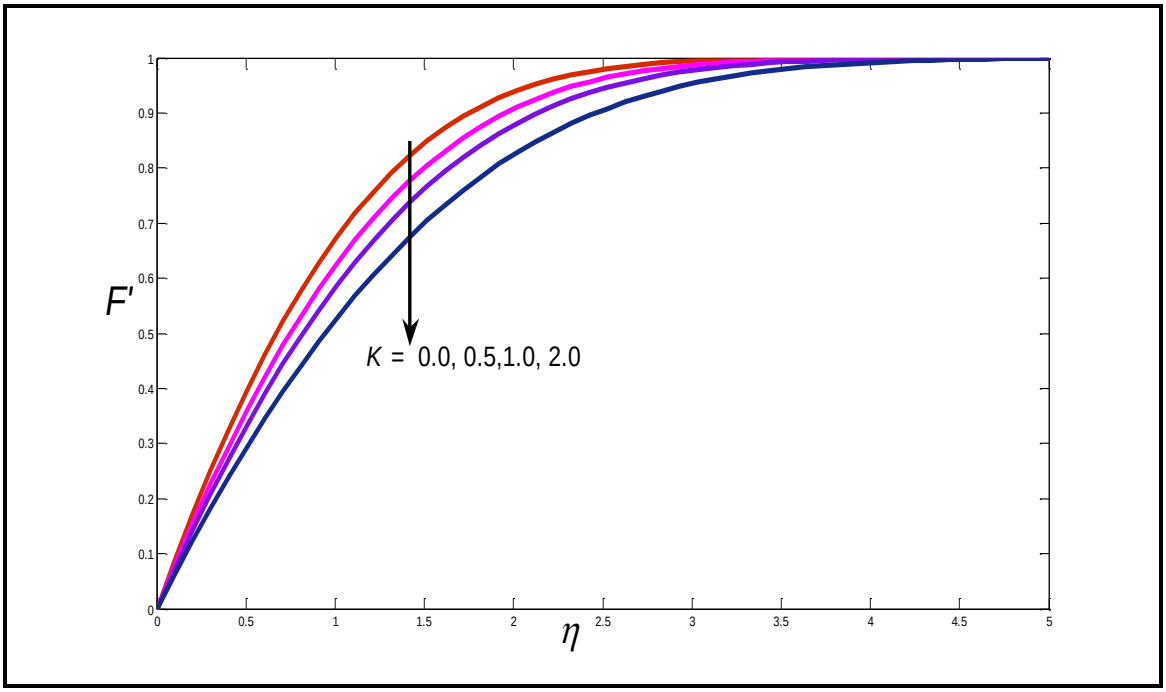

(b)

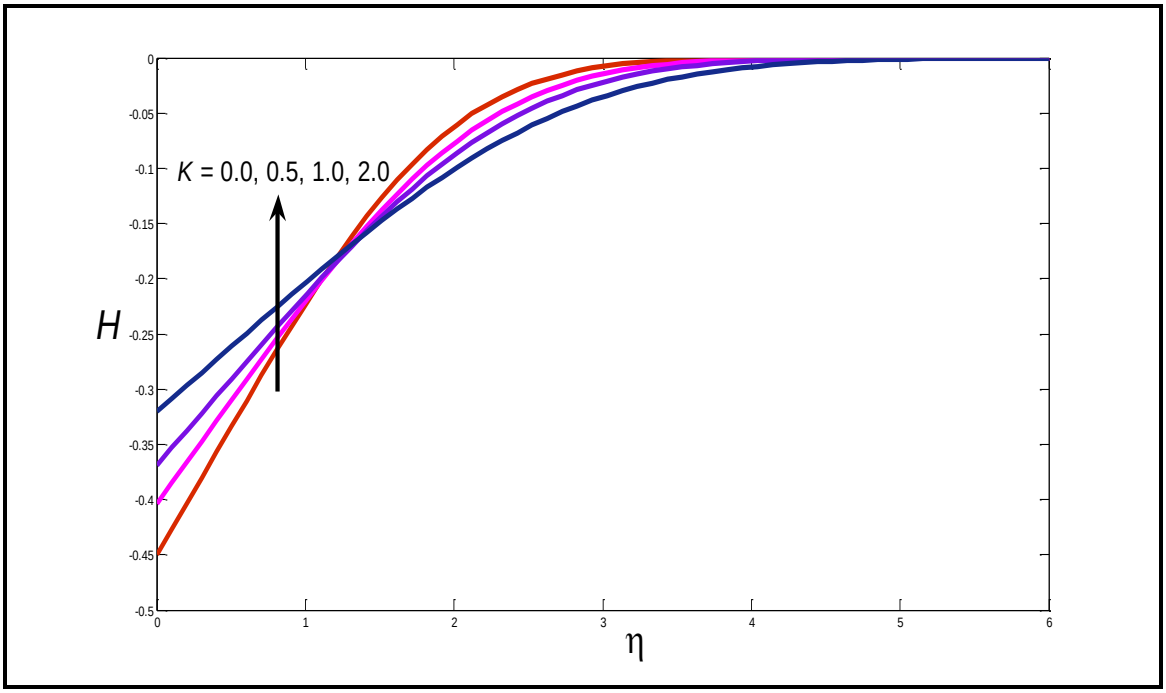

(c)

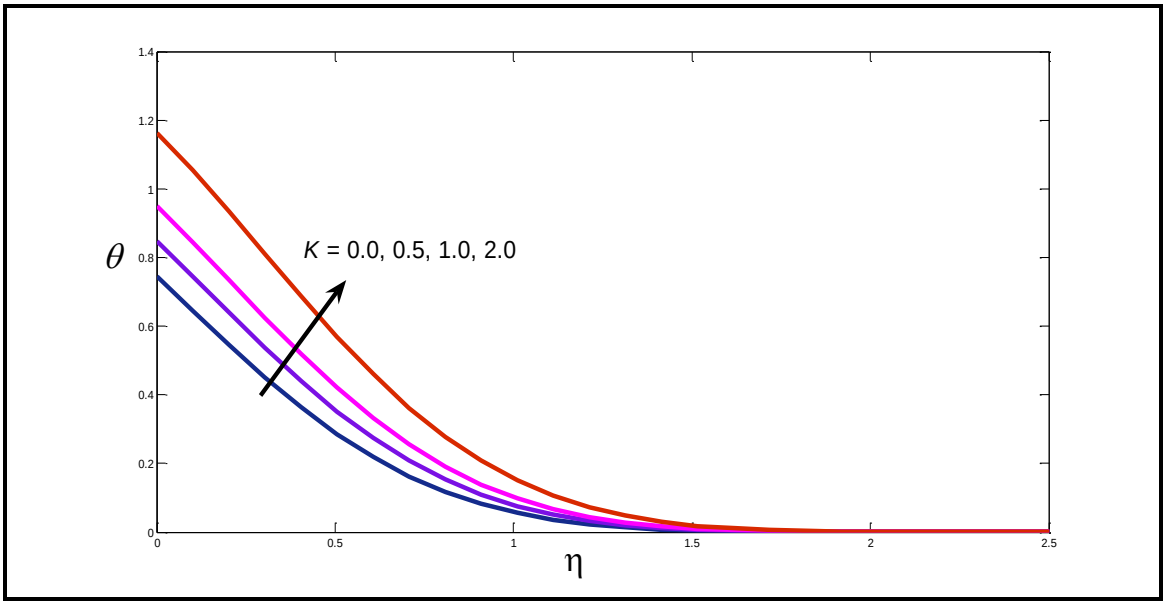

Figure 3. Profiles for (a) primary velocity (F') (b) angular velocity (H) and (c) temperature (θ) for various Eringen micropolar material parameter values (K)

(a)

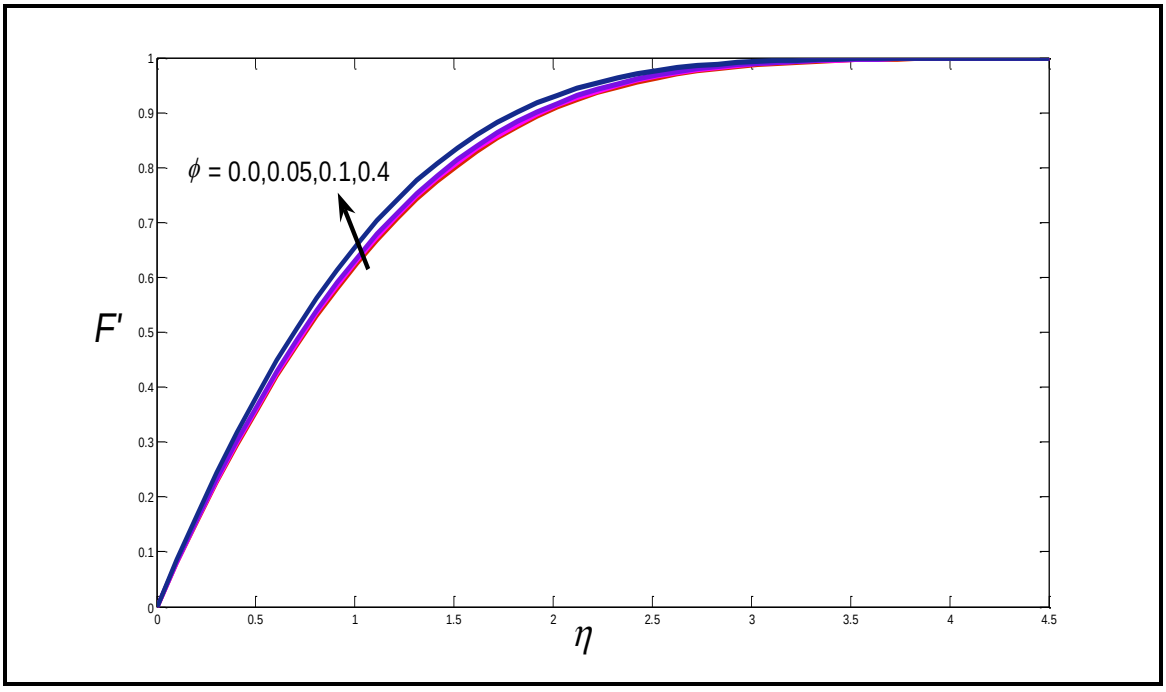

(b)

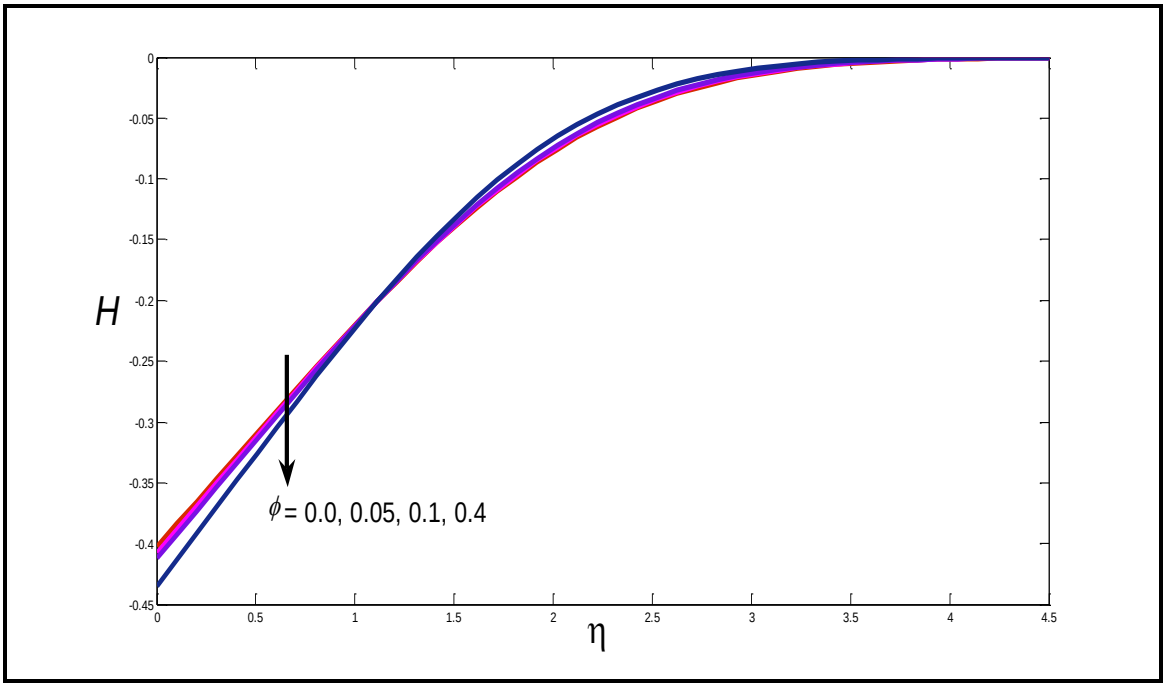

(c)

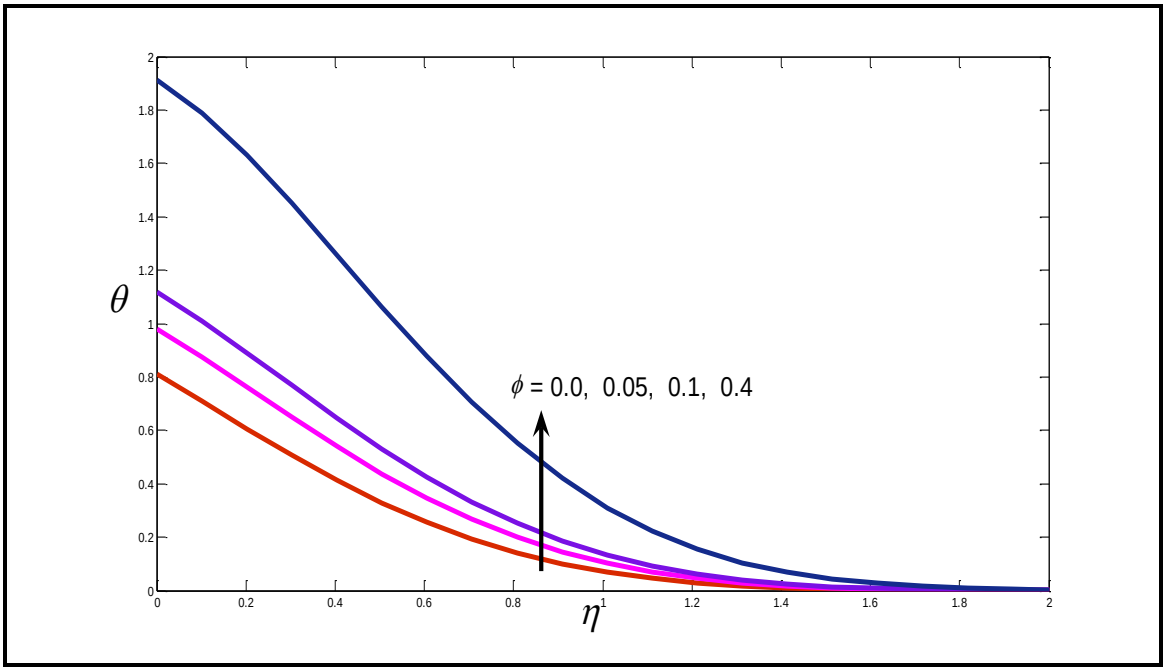

Figure 4. Profiles for (a) primary velocity (F') (b) angular velocity (H) and (c) temperature (θ) for various nanoparticle volume fractions (ϕ) (copper nanoparticles in water)

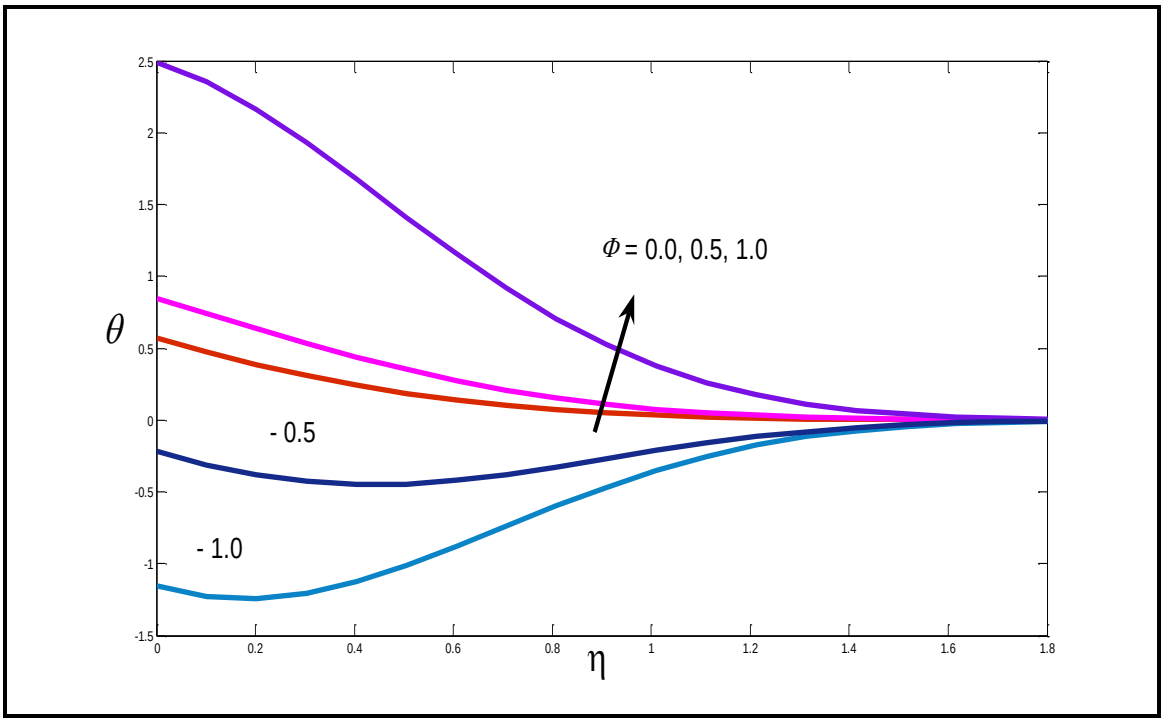

Figure 5. Profiles for temperature (θ) for various heat source/sink parameter values (Φ)

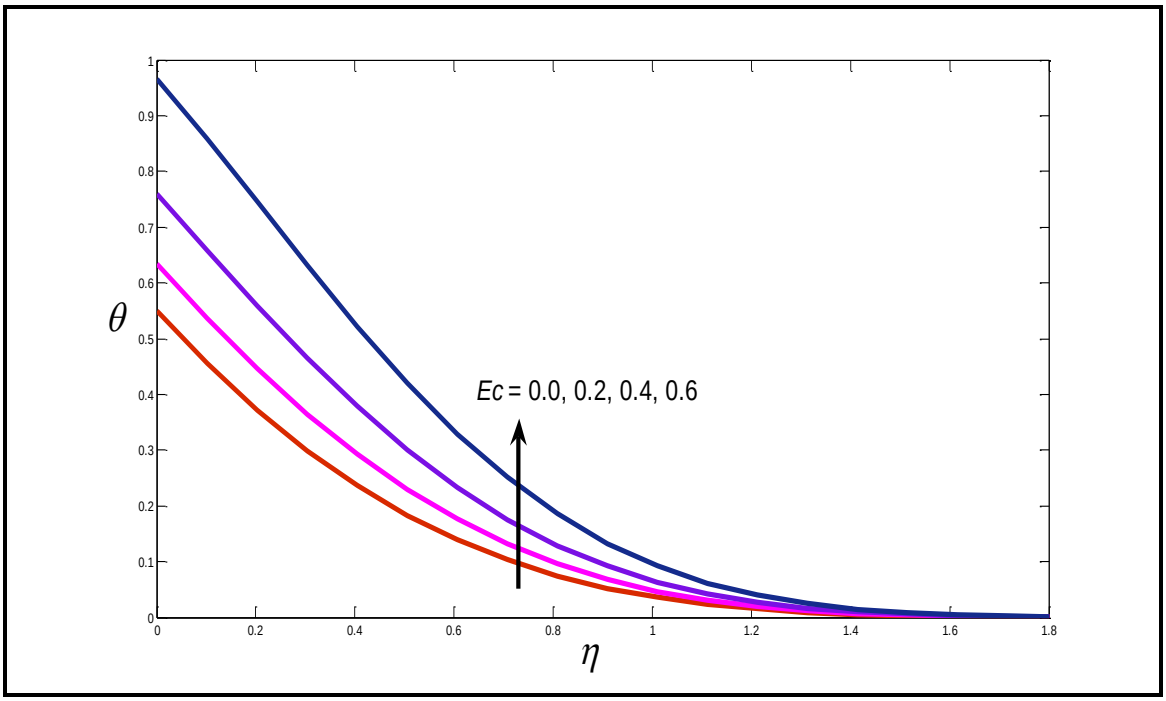

Figure 6. Profiles for temperature (θ) for various Eckert number values (Ec)

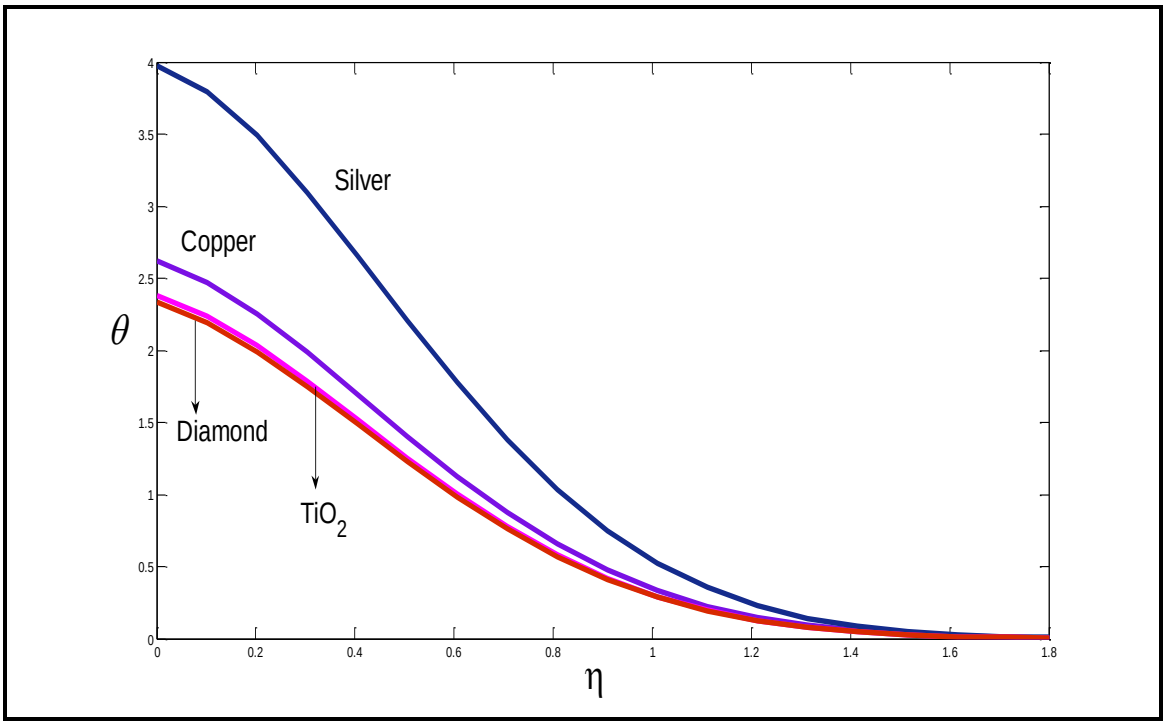

Figure 7. Profiles for temperature (θ) for various nanoparticle types ($\phi = 0.01$ i. e. 1% doping)

Table 1: Comparison of solutions for $\frac{C_{fx}\sqrt{\mathrm{Re}}}{2}$ with

Yi	Chamkha et al. [49]	Ishak et al. [50]	Uddin et al. [30]	Present
0.332057	0.332206	0.3321	0.3466	0.332057

Table 2: Values of $\frac{Nu}{\sqrt{\mathrm{Re}}}$ for

Pr	Lin and Lin [51]	Ishak et al. [50]	Uddin et al. [30]	Present
1	0.45897	0.4590	0.460439	0.458981
10	0.99789	0.9980	1.00012	0.997893
100	2.15197	2.1520	2.163009	2.15201
1000	4.63674	4.6367	4.647032	4.63707

Table 3: Values of $\frac{C_{fx}\sqrt{\mathrm{Re}}}{2}$ and $\frac{Nu}{\sqrt{\mathrm{Re}}}$ for

$I = 0.5,\ \phi = 0.01,\ K = 0.5,\ m = 0.3333,\ \Phi = -0.5,\ Ec = 0.5,\ \mathrm{Pr} = 6.0$

(water as base fluid, copper nanoparticles, unless otherwise indicated)

	$\frac{C_{fx}\sqrt{\mathrm{Re}}}{2}$	$\frac{Nu}{\sqrt{\mathrm{Re}}}$
m		
0.0	0.360924	1.26459
0.3333	0.823263	0.945399
1.0	1.33973	0.218181
K		
0.0	0.738176	1.09174
0.5	0.823263	0.945399
1.0	0.900336	0.830457
ϕ		
0.0	1.01618	0.95743
0.01	0.823263	0.945399
0.1	0.817408	0.827865
Nano Particles	Water as Base fluid	
Copper	0.823263	0.945399
Silver	0.817336	0.944306
Diamond	0.844818	0.949622
TiO2	0.841777	0.947498

5. Conclusions

As a simulation of nano-polymeric coating flow, laminar, steady-state, incompressible nonlinear convective boundary layer flow of a non-Newtonian nanofluid external to a wedge-shaped configuration has been studied theoretically. The wedge surface is assumed to be isothermal.

Viscous dissipation and heat generation/absorption effects are included. The Eringen micropolar model is deployed for rheological characteristics of the nanofluid. A Tiwari-Das nanoscale formulation is utilized in order to study specific nanoparticles and volume fraction effects. The dimensionless, transformed, coupled momentum, angular momentum (micro-rotation) and thermal boundary layer equations with associated wall and free stream conditions are solved with the efficient MATLAB bvp4c numerical scheme. Excellent correlation with previous studies from the literature for special cases of the general model is achieved. Aqueous-based nano-polymers are examined with either metallic/metallic oxide (copper, silver, titania) or carbon-based (diamond) nanoparticles. The main findings of the present computations can be summarized as follows:

(i)Temperature is strongly elevated with increasing micropolar parameter and nanoparticle volume fraction.

(ii)Angular velocity (micro-rotation) is damped near the wedge surface with increment in volume fraction but further from the wall the reverse effect is observed.

(iii) Primary velocity is boosted throughout the boundary layer transverse to the wall with increasing nanoparticle volume fraction.

(iv)Temperatures and thermal boundary layer thicknesses are elevated with heat source (generation) but suppressed with heat sink (absorption).

(v)Increasing Eckert number (dissipation) markedly boosts temperature and thermal boundary layer thickness.

(vi)Temperatures are a maximum for silver and progressively lower for copper, diamond and with a minimum computed for titania.

(vii) Skin friction is boosted with pressure gradient parameter whereas Nusselt number is depleted.

(viii) Highest heat transfer rate to the wall is achieved for the Blasius flow case whereas the minimum heat transfer rate to the wall is produced for the forward stagnation flow case. The wedge case lies between these two extremities.

(ix) An increase in micropolar material parameter, induces a strong increase in primary skin friction whereas it depletes the Nusselt number magnitudes for the wedge case ($m = 0.3333$ with 1% nanoparticle doping).

(x) Both primary skin friction and Nusselt number are depleted with increment in nanoparticle volume fraction, ϕ.

(xi)Nusselt number is maximum for diamond whereas it is a minimum for silver. Copper however also achieves quite high Nusselt number whereas titania produces much lower magnitudes than diamond or copper nanoparticles.

The present study has revealed some interesting insights into micropolar (rheological) nanofluid coating flows with both metallic/oxide and carbon (diamond) nanoparticles using MATLAB bvp4c and the Tiwari-Das nanoscale and Eringen non-Newtonian models. Future studies may consider alternative non-Newtonian models e. g. viscoelastic model, and also different nanoparticles such as magnesium oxide, silicon carbide and zinc oxide. Efforts in these directions will be reported imminently.

Conflict of Interest: The authors do not have any conflict of interest.

Nomenclature

c	Positive constant
c_i	Arbitrary constants
c_p	Specific heat at constant pressure
c_{fx}	Dimensionless primary skin friction
c_{fz}	Dimensionless secondary skin friction
Ec	Eckert number
$F(\eta)$	Dimensionless stream function
$G(\eta)$	Dimensionless secondary velocity
$H(\eta)$	Dimensionless angular velocity
I	Dimensionless Micro-inertia density
j	Micro-inertia density
K	Thermal conductivity
K_f	Thermal conductivity of the fluid

K_s Thermal conductivity of the solid particle

m Hartree pressure gradient

N Angular velocity

NU Nusselt number

Pr Prandtl number

Q Heat sink parameter

q_w Rate of heat transfer

Re Reynolds number

T Fluid temperature

T_∞ Ambient fluid temperature

u Velocity along the $x-$direction

$U = c\,x^m$ External velocity

v Velocity along $y-$direction

x, y, z Cartesian coordinates

Greek Symbols

$\alpha,\ \beta$ Spin gradient viscosity co-efficients

$\gamma = \left(\mu + \frac{\kappa}{2}\right) j$ Eringen spin gradient viscosity

μ Dynamic viscosity

λ Eringen second order viscosity coefficient

ρ Mass density of micropolar fluid

κ Vortex viscosity

$\theta(\eta)$ Dimensionless temperature

η Pseudo similarity coordinate in the $y-$direction

τ_x Primary dimensional wall shear stress

τ_z Secondary dimensional wall shear stress

Φ Heat sink parameter

$\Omega = \beta^*\ \pi$ Total vertex angle of the wedge

Subscripts

nf	Nanofluid
f	Base fluid
s	Solid nanoparticles
w	Wall condition
∞	Ambient condition

Superscript

‘	Prime denotes the derivative with respect to η

References

[1] Hussain CM. Handbook of Nanomaterials for Industrial Applications. Elsevier, USA; 2018.

[2] Das SK, Choi SUS, Patel HE. Heat transfer in nanofluids - a review. Heat Transfer Engineering. 2006; 27:3-19.

[3] Königer T et al. CO_2-laser treatment of indium tin oxide nanoparticle coatings on flexible polyethyleneterephthalate substrates. J. Coatings Technology and Research. 2010; 7:261–269.

[4] Phan HT et al. Surface coating with nanofluids: the effects on pool boiling heat transfer. Nanoscale and Microscale Thermophysical Engineering. 2010;14:229-244.

[5] Goebbert C, Nonninger R, Aegerter MA, Schmidt H. Wet chemical deposition of ATO and ITO coatings using crystalline nanoparticles redispersable in solutions. Thin Solid Films. 1999; 351:79-84.

[6] Atayev P, Oner M. Effect of incorporation of clay and zinc oxide nanoparticles on oxygen barrier properties of polypropylene sheet. J. Plast. Film Sheet. 2014;30:248–265.

[7] Sanchez-Garcia MD, Ocio MJ, Gimenez E et al. Novel polycaprolactone nanocomposites containing thymol of interest in antimicrobial film and coating applications. J. Plast. Film Sheet. 2008;24:239–251.

[8] Buongiorno J. Convective transport in nanofluids. A.S.M.E. J. Heat Transfer. 2006;128: 240–250.

[9] Tiwari RJ, Das MK. Heat transfer augmentation in a two-sided lid-driven differentially heated square cavity utilizing nanofluids. Int. J. Heat Mass Transfer. 2007;50:2002-2018.

[10] Minkowycz WM, Sparrow EM, Abraham JP. Nanoparticle Heat Transfer and Fluid Flow. CRC Press; Florida : 2013.

[11] Khaliq S, Abbas Z. A theoretical analysis of roll-over-web coating assessment of viscous nanofluid containing Cu-water nanoparticles. J. Plast. Film Sheet. 2019;36:55-75.

[12] Ahmadian A et al. Numerical analysis of thermal conductive hybrid nanofuid flow over the surface of a wavy spinning disk. Scientific Reports. 2020;10:18776.

[13] Karim MK et al. Performance of Graphite-Dispersed Li_2CO_3-K_2CO_3 Molten Salt Nanofluid for a Direct Absorption Solar Collector System. Molecules. 2020;25:375.

[14] Kim S, Kim C, Lee WY, Park SR. Rheological properties of alumina nanofluids and their implication to the heat transfer enhancement mechanism. J. Appl. Phys. 2011;110:034316.

[15] Rawat SK, Upreti H, Kumar M. Numerical study of activation energy and thermal radiation effects on oldroyd-b nanofluid flow using the Cattaneo–Christov double diffusion model over a convectively heated stretching sheet. Heat Transfer. 2021;50:5304-5331.

[16] Umavathi JC, Bég OA. Simulation of the onset of convection in porous medium layer saturated by a couple stress nanofluid. Microfluidics and Nanofluidics. 2021;25:53-73.

[17] Eringen AC. Theory of micropolar fluids. J. Math. Mech. 1966;16:1-18.

[18] Ali N, Asghar Z, Bég OA. A mathematical model of bacterial gliding on a thin layer of micropolar slime. Results in Physics. 2018;9:682-691.

[19] Bég OA, Zueco J, Chang TB. Numerical analysis of hydromagnetic gravity-driven thin film micropolar flow along an inclined plane, Chemical Engineering Communications. 2010;198:312- 331.

[19] Reddy GJ, Kethireddy B, Bég OA. Flow visualization using heat lines for unsteady radiative hydromagnetic micropolar convection from a vertical slender hollow cylinder. Int. J. Mechanical Sciences. 2018;140:493-505.

[20] Shamshuddin MD, Sheri SR, Bég OA. Oscillatory dissipative conjugate heat and mass transfer in chemically reacting micropolar flow with wall couple stress: A finite element numerical study. Proc. IMechE Part E: J. Process Mechanical Engineering. 2019;233:48-64.

[21] Madhavi K, V. Ramachandra Prasad, A. Subba Rao, O. Anwar Bég and A. Kadir, Numerical study of viscoelastic micropolar heat transfer from a vertical cone for thermal

polymer coating. Nonlinear Engineering. DOI.ORG/10.1515/NLENG-2018 2018-0064 REC (13 pages)

[22] Abdul Gaffar, B.M.H. Khan, O. Anwar Bég, A. Kadir, P.M. Reddy, Computation of Eyring-Powell micropolar convective boundary layer flow from an inverted non-isothermal cone: thermal polymer coating simulation. Computational Thermal Sciences. 2020;12:329–344.

[23] Latiff NA, Uddin MJ, Bég OA, Ismail AIM. Unsteady forced bioconvection slip flow of a micropolar nanofluid from a stretching/ shrinking sheet. Proc. IMechE- Part N: J. Nanoengineering and Nanosystems. 2016;230:177–187.

[24] Gumber P et al. Heat transfer in micropolar hybrid nanofluid flow past a vertical plate in the presence of thermal radiation and suction/injection effects. Partial Differential Equations in Applied Mathematics. 2022;5:100240.

[25] Das K, Duari PK. Micropolar nanofluid flow over an stretching sheet with chemical reaction. International Journal of Applied and Computational Mathematics. 2017;3:3229–3239.

[26] Hussanan A et al. Convection heat transfer in micropolar nanofluids with oxide nanoparticles in water, kerosene and engine oil. Journal of Molecular Liquids. 2017;229: 482-488.

[27] Falkner VM, Skan SW. Aero. Res. Coun. Rep. and Mem. 1930; 1314.

[28] Rosenhead. Laminar Boundary Layers. Louis (Ed) Clarendon Press; Oxford: 1963.

[29] Ramesh Reddy P, Abdul Gaffar S, Hidayathulla Khan BM, Venkatadri K, Bég OA. Mixed convection flows of tangent hyperbolic fluid past an isothermal wedge with entropy: A mathematical study. Heat Transfer. 2020; DOI: 10.1002/htj.22011 (34 pages).

[30] Uddin Z, Kumar M, Harmand S. Influence of thermal radiation and heat generation/ /absorption on MHD heat transfer flow of a micropolar fluid past a wedge with Hall and ion slip currents. Thermal Science. 2014;18:S489-S502.

[31] Bég OA, Vasu B, Ray AK, Bég TA, Kadir A, Leonard JJ, Gorla RSR. Homotopy simulation of dissipative micropolar flow and heat transfer from a two-dimensional body with heat sink effect: applications in polymer coating. Chem. Biochem. Eng. Quart. 2020;34:257–275.

[32] Gaffar SA, Prasad VR, Kumar BR, Bég OA. Computational modelling and solutions for mixed convection boundary layer flows of nanofluid from a non-isothermal wedge. J. Nanofluids 2018;7:1–9.

[33] Xu X, Chen S. Dual solutions of a boundary layer problem for MHD nanofluids through a permeable wedge with variable viscosity. Bound. Val. Prob. 2017;147.

[34] Uddin MJ, Kabir MN, Bég OA, Alginahi Y. Chebyshev collocation computation of magneto-bioconvection nanofluid flow over a wedge with multiple slips and magnetic induction. Proc. IMechE: Part N-Journal of Nanomaterials, Nanoengineering and Nanosystems. 2018;232: 109-122.

[35] Tulu A, Ibrahim W. Numerical analysis of heat and mass transfer flow of nanofluid over a moving wedge using spectral quasilinearization method. International Journal of Applied Mathematics and Theoretical Physics. 2019;5:111-117.

[36] Khan U, Ahmed N, Mohyud-Din ST. Heat transfer enhancement in hydromagnetic dissipative flow past a moving wedge suspended by H_2O–aluminum alloy nanoparticles in the presence of thermal radiation. Int. J. Hydrog. Energy. 2017;42:24344–634.

[37] Ullah I, Shafie S, Khan I, Hsiao KL. Brownian diffusion and thermophoresis mechanisms in Casson fluid over a moving wedge. Results Phys. 2018;9:183–94.

[38] Rauf A, Irfan M, Omar M, Mushtaq T, Shehzad SA, Bashir MN. Numerical study of micropolar nanofluid flow between two parallel permeable disks with thermophysical property and Arrhenius activation energy. Int. Comm. In Heat and Mass Transfer. 2022:137:106272.

[39] Rauf A, Sahar N, Siddiq MK, Mustafa F, Mushtaq T, Shehzad SA. Numerical and correlation analysis for flow of micropolar fluid induced by two rotating disks. Chinese J. of Physics. 2023:83:147-164.

[40] Rauf A, Shehzadi SA, Abbas Z, Hayat T. Unsteady three-dimensional MHD flow of the micropolar fluid over an oscillatory disk with Cattaneo-Christov double diffusion. Appl. Math. Mech. (English Edition). 2019:40:1471-1486.

[41] Nawaz M, et al. Dynamics of slip phenomenon in micropolar nanofluid flowing over a stretchable disk with Arrhenius activation energy. Proceedings of the Inst. Of Mech. Engng., Part E: J. Process Mech. Engng. 2022 https://doi.org/10.1177/09544089221113144.

[42] Mahanthesh B et al. Significance of Joule heating and viscous heating on heat transport of MoS_2–Ag hybrid nanofluid past an isothermal wedge. Journal of Thermal Analysis and Calorimetry. 2021;143:1221–1229.

[43] Petkov V, Valov R. Effects of diamond nanoparticles on the microstructure, hardness and corrosion resistance of chromium coatings. Am. J. Chemical Engineering. 2020;8:125-130.

[44] Petkov V, Valov R, Witkowska M, Madej M, Cempura G, Sułowski M. Sintered steels coated with a chromium layer doped with diamond nanoparticles. Arch. Metall. Mater. 2019; 64: 1633-1638.

[45] Almasi H, Jafarzadeh P, Mehryar L. Fabrication of novel nanohybrids by impregnation of CuO nanoparticles into bacterial cellulose and chitosan nanofibers: Characterization, antimicrobial and release properties. Carbohydr. Polym. 2018;186:273–281.

[46] Umavathi JC, Bég OA. Mathematical modelling of triple diffusion in natural convection flow in a vertical duct with Robin boundary conditions, viscous heating and chemical reaction effects. J. Engineering Thermophysics. 2020;29:1–26.

[47] Umavathi JC, Patil SL, Mahanthesh B, Bég OA. Unsteady squeezing flow of magnetized nano-lubricant between parallel disks with Robin boundary condition. Proc. IMechE J. Nanomaterials Nanoengineering, Nanosystems. 2020; DOI: 10.1177/23977914211036562 (15 pages)

[48] Kattan PI. Matlab For Beginners. CreateSpace Independent Publishing Platform; USA: 2008.

[49] Chamka AJ et al. Thermal radiation effects on MHD forced convection flow adjacent to a non-isothermal wedge in the presence of heat source or sink. Heat Mass Transfer. 2003;39: 305-312.

[50] Ishak A et al. MHD boundary-layer flow of a micropolar fluid past a wedge with constant wall heat flux. Comm. Nonlinear Science Num. Simulation. 2009;14:109-118.

[51] Lin HT, Lin LK. Similarity solutions for laminar forced convection heat transfer from wedges to fluids of any Prandtl number. Int. J. Heat Mass Transfer. 1987;6:1111-1118.

[52] Hussain CM, Thomas S. Handbook of Polymer and Ceramic Nanotechnology. Springer Nature; Switzerland: 2020.